J Nanopart Res (2011) 13:4717–4729
DOI 10.1007/s11051-011-0439-3

RESEARCH PAPER

Multifunctional iron platinum stealth immunomicelles: targeted detection of human prostate cancer cells using both fluorescence and magnetic resonance imaging

Robert M. Taylor · Dale L. Huber · Todd C. Monson · Abdul-Mehdi S. Ali · Marco Bisoffi · Laurel O. Sillerud

Received: 26 December 2010 / Accepted: 26 May 2011 / Published online: 11 June 2011

Abstract Superparamagnetic iron oxide nanoparticles (SPIONs) are the most common type of contrast agents used in contrast agent-enhanced magnetic resonance imaging (MRI). Still, there is a great deal of room for improvement, and nanoparticles with increased MRI relaxivities are needed to increase the contrast enhancement in MRI applied to various medical conditions including cancer. We report the synthesis of superparamagnetic iron platinum nanoparticles (SIPPs) and subsequent encapsulation using PEGylated phospholipids to create stealth immunomicelles (DSPE-SIPPs) that can be specifically targeted to human prostate cancer cell lines and detected using both MRI and fluorescence imaging. SIPP cores and DSPE-SIPPs were 8.5 ± 1.6 nm and 42.9 ± 8.2 nm in diameter, respectively, and the SIPPs had a magnetic moment of 120 A m^2/kg iron. J591, a monoclonal antibody against prostate specific membrane antigen (PSMA), was conjugated to the DSPE-SIPPs (J591-DSPE-SIPPs), and specific targeting of J591-DSPE-SIPPs to PSMA-expressing human prostate cancer cell lines was demonstrated using fluorescence confocal microscopy. The transverse relaxivity of the DSPE-SIPPs, measured at 4.7 Tesla, was 300.6 ± 8.5 s^{-1} mM^{-1}, which is 13-fold better than commercially available SPIONs (23.8 ± 6.9 s^{-1} mM^{-1}) and ~3-fold better than reported relaxivities for Feridex® and Resovist®. Our data suggest that J591-DSPE-SIPPs specifically target human prostate cancer cells in vitro, are superior contrast agents in T_2-weighted MRI, and can be detected using fluorescence imaging. To our knowledge, this is the first report on the synthesis of multifunctional SIPP micelles and using SIPPs for the specific detection of prostate cancer.

Keywords Iron platinum · Micelle · Prostate cancer · Contrast agent · Magnetic resonance imaging · Fluorescent nanoparticle · Nanomedicine

R. M. Taylor (✉) · M. Bisoffi · L. O. Sillerud
Department of Biochemistry and Molecular Biology, University of New Mexico School of Medicine, Albuquerque, NM 87131, USA
e-mail: rmtaylor@salud.unm.edu

D. L. Huber
Center for Integrated Nanotechnologies, Sandia National Laboratories, Albuquerque, NM 87111, USA

T. C. Monson
Nanomaterials Sciences Department, Sandia National Laboratories, Albuquerque, NM 87111, USA

A.-M. S. Ali
Department of Earth and Planetary Sciences, University of New Mexico, Albuquerque, NM 87131, USA

Introduction

In the United States, prostate cancer is the second most common reason for cancer death in men (Jemal et al. 2010). Accurate detection methods are important for all aspects of the clinical management of

prostate cancer, including diagnosis, risk assessment, staging, and prognosis. Such methods will result in individualized and efficacious treatments for patients at risk for prostate cancer or for its progression. Many of these tasks are currently managed by determination of the serum biomarker prostate specific antigen (PSA). For example, serum PSA levels are employed to evaluate prostate cancer risk and progression, and justify confirmatory biopsies to diagnose the presence of malignancy. However, biopsies have inherent risks such as bleeding and infection (Andrew et al. 2010), and cancer is not detected (false negative cases) in 30–50% of biopsies in patients with subsequently confirmed malignancy due to small and inconspicuous lesions (Rabbani et al. 1998). Another major issue is that ~25–40% of patients are over diagnosed using current detection methods leading to superfluous biopsies (Andrew et al. 2010). These findings indicate that the detection and staging of prostate cancer needs to be improved. Novel magnetic resonance molecular imaging methods promise to markedly increase the specificity of prostate tumor detection (Afnan and Tempany 2010).

Our goal is to develop targeted magnetic resonance imaging (MRI) agents for the specific detection of prostate cancer. A unifying theme in the development of novel imaging and therapeutic modalities in recent years has been specifically targeting these agents to cells of interest (Peng et al. 2008). The targeting motifs are often antibodies against antigens expressed on cancerous cells but not healthy cells. The most promising target antigen expressed specifically on prostate cancer cells is prostate specific membrane antigen (PSMA), which is most strongly expressed in the prostate, and expression has been found to increase as tumor grade and stage increases (Rajasekaran et al. 2005). In addition, many nonprostatic tumors have been found to express PSMA in the neovasculature, but expression in healthy vasculature has not been reported (Ghosh and Heston 2004; Chang et al. 1999), suggesting that PSMA may also be a general tumor antigen that could be used to detect numerous types of solid tumors. Thus, antibodies against PSMA are an appealing choice for use as targeting motifs for prostate cancer.

Superparamagnetic iron oxide nanoparticles (SPIONs) are the most common type of contrast agents used in agent-enhanced MRI (Zhang et al. 2010). Although SPIONs cause negative contrast in the MR images, the signal enhancement is still lower than other common imaging techniques (Lee et al. 2007). Therefore, novel nanoparticles with increased MRI relaxivities are needed to increase the signal enhancement in MRI and the detection of cancer, using lower doses of the contrast agents. Iron platinum (FePt) particles have been the focus of intense research in recent years due to their high magnetic anisotropy and high stability (Han et al. 2009; Kim et al. 2009; Antoniak et al. 2006; Sun 2006; Sun et al. 2000). Much of the interest in FePt has been placed on producing ferromagnetic face-centered tetragonal (fct) FePt particles, for use in magnetic storage devices, by annealing superparamagnetic face-centered cubic (fcc) nanoparticles at temperatures exceeding 500 °C (Basit et al. 2009; Varanda and Jafelicci 2006; Boyen et al. 2005; Sun et al. 2000). However, fcc superparamagnetic iron platinum particles (SIPPs) are of interest by themselves due to their possible use as contrast agents in MRI (Chen et al. 2010; Morales et al. 2009; Maenosono et al. 2008). For superparamagnetic MRI contrast agents, it is thought that a higher magnetic moment at a given magnetic field causes larger perturbations in the magnetic relaxation times of nearby water protons and, thus, higher moment particles should generate increased image contrast. SIPPs have previously been reported with volume magnetizations greater than 590 emu/cm^3 (6×10^5 A m^2), with some preparations approaching 1.140 emu/cm^3 (1×10^6 A m^2), the saturation magnetization of bulk FePt (Xu et al. 2009; Zhao et al. 2009; Barmak et al. 2004; Zeng et al. 2002). These reported high magnetic moments suggested that SIPPs would be superior MRI contrast agents.

One obvious drawback to the synthesis of various types of nanoparticles is that toxic precursors are generally employed to produce the particles (Sun 2006; Sun et al. 2000; Inomata et al. 1988). Often, iron pentacarbonyl, $Fe(CO)_5$, a very hazardous reagent (Bhalerao et al. 2009), is used as the iron precursor in FePt syntheses (Sun et al. 2000). A number of different FePt syntheses are described by Sun (2006). Recently, Zhao et al. (2009) described a method for producing ~11 nm SIPPs using the hydrophobic surface ligand 1-Octadecylamine (ODA) along with iron and platinum salts that are much less hazardous than $Fe(CO)_5$. In this article, we report the synthesis of SIPP cores using modifications

of this less hazardous method. In order to use hydrophobic core nanoparticles in vivo, the particles must first be made biocompatible. A plethora of methods for encapsulating drugs and hydrophobic imaging agents, to instill biocompatibility, have been reported and include encapsulation using hydrophilic or amphiphilic components such as monomers and phospholipids (Serda et al. 2010). In addition, polyethylene glycol (PEG) groups on nanoparticles have been shown to increase solubility and circulation times and decrease immunogenicity (Serda et al. 2010; Pasut and Veronese 2009). This decrease in immunogenicity imparts the nanoparticles with stealth capability in vivo. Furthermore, biocompatible contrast agents that also incorporate a fluorescent component offer the advantage of in vivo and ex vivo imaging using small animal fluorescence imagers and/or fluorescence microscopy for in vivo biodistribution studies and in vitro binding assays. In this article, we describe the physical and magnetic characterization of SIPP cores encapsulated with a mixture of 1,2-distearoyl-sn-glycero-3-phosphoethanolamine-*N*-[amino(polyethylene glycol)-2000] (DSPE-PEG), DSPE-PEG with biotin conjugated to the head group (biotin-DSPE-PEG), 1,2-dimyristoyl-sn-glycero-3-phosphoethanolamine-*N*-[lissamine rhodamine B sulfonyl] (Liss-Rhod), and subsequent conjugation to a monoclonal antibody (J591) against PSMA (J591-DSPE-SIPPs). In this study, we also demonstrate the specific binding of J591-DSPE-SIPPs to PSMA-positive prostate cancer cells using confocal microscopy and measure the MR relaxivities of the DSPE-SIPPs at 4.7 Tesla. Compared to the commercially available and clinically used SPIONs, the J591-DSPE-SIPPs are superior contrast agents in T_2-weighted MRI, specifically target PSMA-positive human prostate cancer cells, and can be detected with fluorescence microscopy. To our knowledge, this is the first report on the synthesis of multifunctional SIPP micelles and the first report of using SIPPs for the specific detection of prostate cancer cells.

Experimental details

Materials

Iron nitrate nonahydrate ($Fe(NO_3)_3{\cdot}9H_2O$), Platinum (II) acetylacetonate ($Pt(Acac)_2$), and ODA were purchased from Fisher Scientific (Pittsburgh, PA). Temperature controller (model 210-J) was purchased from J-KEM Scientific, INC (St. Louis, MO). Heating mantle was purchased from Glas-Col, LLC (Terre Haute, IN), and glassware was purchased from Quark Glass (Vineland, NJ). The phospholipids 1,2-distearoyl-sn-glycero-3-phosphoethanolamine-*N*-[amino(polyethylene glycol)-2000] (DSPE-PEG), DSPE-PEG with biotin conjugated to the head group (biotin-DSPE-PEG), and 1,2-dimyristoyl-sn-glycero-3-phosphoethanolamine-*N*-[lissamine rhodamine B sulfonyl] (Liss-Rhod) were purchased from Avanti Polar Lipids (Alabaster, AL). SPIONs were purchased from Miltenyi Biotec (Carlsbad, CA) as their MACS® Streptavidin MicroBeads product. RPMI cell culture media, fetal bovine serum, and Penicillin–Streptomycin Solution were purchased from Sigma (St. Louis, MO). All other chemicals and supplies were purchased from common manufacturers.

Synthesis of SIPP cores

Nanoparticles were synthesized using a modification of a procedure Zhao et al. (2009). In brief, 1.0 mmol $Fe(NO_3)_3{\cdot}9H_2O$ and 1.0 mmol $Pt(Acac)_2$ were added to 12.5 mmol ODA in a 25 mL 3-neck round bottom flask fitted with a reflux condenser. The reaction was heated to 330 °C (200 °C/h) with 10 °C recirculated cooling in the reflux condenser. Refluxing was continued for 45 min at which point the reaction was removed from the heat and allowed to cool to room temperature. The resulting black particles were collected in hexane and subjected to repeated washing by collecting particles in conical tubes with an external magnet, removing the supernatant, and resuspending in hexane.

Encapsulation of SIPP cores

Phospholipid-encapsulated SIPP cores (DSPE-SIPPs) were prepared using a thin film method. 1.5 mL of SIPP cores (1.4% solids) in hexane was added to a 20.0 mL glass scintillation vial. A chloroform mixture of (56:1:1 mol ratio) DSPE-PEG, biotin-DSPE-PEG, and Liss-Rhod was then added to the SIPP cores. The mixture was further diluted in 1.5 mL of hexane and vortexed thoroughly. The vial was wrapped in aluminum foil and allowed to evaporate in the dark in a chemical fume hood overnight to

produce a thin film. 5.0 mL of double-distilled water was heated to 67 °C and added to the thin film. Hydration of the thin film was then continued in a 67 °C water bath for 1.0 h with vortexing every 15 min to produce liposomes containing SIPP cores. The liposomes were then extruded at 67 °C through an 80-nm nuclepore track-etch membrane filter using a mini-extruder (Avanti Polar Lipids, Alabaster, AL) to produce ~45 nm DSPE-SIPP micelles. The DSPE-SIPPs were then purified from SIPP-free micelles and excess phospholipids by collecting the magnetic particles using an LS magnetic column placed in a VarioMACS™ magnetic separator (Miltenyi Biotec, Carlsbad, CA). After the non-magnetic material had passed through the column, 8.0 mL of double-distilled water was added to the top of the column to wash the particles. The washing was then repeated a second time. The column was removed from the magnet and placed in a tube rack with a 2.0 mL glass vial placed underneath the column. 2.0 mL of either double-distilled water or phosphate buffered saline (PBS), pH 7.4, was used to elute the purified DSPE-SIPPs from the column.

Physical characterization of SIPP cores and DSPE-SIPPs

Transmission electron microscopy (TEM) was utilized to determine the size and polydispersity of the particle populations. For SIPP cores, a drop of the hexane suspension was applied to a carbon-coated grid and dried. For DSPE-SIPPs, a drop of the aqueous suspension was applied to a carbon-coated grid, dried for 10 min, and the excess was absorbed using a kimwipe. Adding a drop of 2% Uranyl Acetate solution followed by a 2-min drying period negatively stained the grid. The excess was removed, and the grid was allowed to dry for at least 5 min. The samples were imaged on a Hitachi 7500 TEM with an acceleration voltage of 80 kV. Particle diameters were calculated using ImageJ Software (Rasband 1997–2009). At least 1000 particles were counted, and the mean Feret diameters and standard deviations were calculated. Diameters of the DSPE-SIPPs were additionally measured using Dynamic Light Scattering (DLS) with a Microtrac Nanotrac™ Ultra DLS (Microtrac, Largo, FL). The compositions of the SIPPs, phospholipids, and DSPE-SIPPs were investigated with thermogravimetric analysis (TGA). Aliquots of ODA, SIPP cores, phospholipids, or DSPE-SIPPs were placed in the TGA sample cup and evaporated at 30 °C under an argon stream for at least 90 min until all solvent had been removed and the mass of the sample stabilized. Weight loss profiles were then measured with a Pyris™ 1 thermogravimetric analyzer (PerkinElmer, Waltham, MA) under argon flow. The ODA, phospholipid, and SIPP content were determined by measuring the mass loss profile while the temperature was raised from 30 to 1000 °C at a 10 °C/min ramp rate. Inductively coupled plasma-optical emission spectroscopy (ICP-OES) was used to measure the metal content and iron to platinum ratio of each synthesis. Before analysis, aliquots of the particles were digested at 180 °C with nitric and hydrochloric acids in a PDS-6 Pressure Digestion System (Loftfields Analytical Solutions, Neu Eichenberg, Germany). After cooling, the samples were made up to a known volume, mixed, and centrifuged. Samples were then analyzed using a PerkinElmer Optima 5300DV ICP-OES. The recommended wavelengths for each of the analytes were used, and analysis was performed in an axial mode to improve detection limits. A blank and set of calibration standards were used to establish a three-point calibration curve. Calibration and instrument verification samples were analyzed before and after analyzing the samples, as well as periodically throughout the measurements. Analyte peaks were examined and peak identification and background points were adjusted for optimum recoveries.

Magnetic characterization of SIPP cores and DSPE-SIPPs

Superconducting quantum interference device (SQUID) magnetometry was employed to measure the blocking temperatures of the SIPP cores, DSPE-SIPPs, and MACS® SPIONs and saturation magnetizations of the SIPPs and MACS® SPIONs. An aliquot (100 μL) of the samples were applied to the end of cotton Qtips® (Unilever, Englewood Cliffs, NJ). Magnetic measurements were then made on a Quantum Design MPMS-7 SQUID magnetometer. Temperature sweeps between 0 and 310 K were performed by zero-field cooling the sample and then measuring the magnetic moment as a function of temperature under the influence of a weak magnetic field (1 mT) during warming and subsequent cooling.

This procedure yields both a zero-field-cooled (ZFC) and field-cooled (FC) curve, respectively. Values of the blocking temperature (T_B) were recorded by determining the peak location in each ZFC curve. Saturation magnetizations were measured at 310 K (37 °C) by varying the applied field from −5 to 5 Tesla. Mass magnetizations were calculated from the known iron concentrations determined by ICP-OES.

Magnetic resonance relaxometry

Increasing concentrations of SPIONs (0.08–0.48 mM iron) or DSPE-SIPPs (0.04–0.20 mM iron) were added to 1% agarose in 2.0 mL self-standing microcentrifuge tubes (Corning, Corning, NY). Samples were imaged on a 4.7 Tesla Bruker Biospin (Billerica, MA) MRI system with Paravision 4.0 software. Samples were imaged with a 256 × 256 matrix, a variable *TE*, and $TR = 10$ s. T_1 measurements were acquired by inversion-recovery with 15 interpulse delays. Spin- and gradient- echo sequences were employed to measure T_2, and T_2*, respectively. The MRI samples were then digested as above, and the iron concentration was determined with ICP-OES. The relaxation rates, $R_n = \frac{1}{T_n}$, were calculated and plotted versus the ICP-OES-determined iron concentration of each sample. Linear regression was used to fit the data, and the relaxivity (r_n) of each sample is given as the slope of the resulting line in units of s^{-1} mM^{-1} of iron.

Antibody conjugation, cell culture, and confocal binding assay

Humanized monoclonal antibody against PSMA (J591) (purchased from Neal Bander, Cornell College of Medicine) and polyclonal goat anti-rabbit IgG (Sigma, St. Louis, MO) were conjugated to streptavidin in an overnight reaction using a Lightning-Link™ Streptavidin Conjugation Kit (Innova Biosciences, Cambridge, UK) according to the manufacturers' instructions. Concentrations of streptavidin, antibodies, and streptavidin-antibody conjugates were quantitated using a NanoDrop™ 2000 Spectrophotometer (Wilmington, DE). Streptavidin-conjugated antibodies (~30 μg) were then incubated with DSPE-SIPPs (100 μg iron) overnight at 4 °C to conjugate the antibodies to the DSPE-SIPPs through the biotin groups of the biotin-DSPE-PEG. A Micro BCA™ Protein Assay (Thermo Scientific, Rockford, IL) was employed to quantitate the antibody concentrations and the amount of antibody conjugated to the DSPE-SIPP surface using a BioSpec-mini Spectrophotometer (Shimadzu, Columbia, MD) at a wavelength of 562 nm. 20,000 C4-2 or PC-3 human prostate cancer cells in RPMI media containing 10% fetal bovine serum and 100 U/mL Penicillin–Streptomycin solution were seeded onto polylysine-coated cover slips in 6-well polystyrene plates (Corning, Corning, NY) and incubated at 37 °C, 5% CO_2 for 24 h. The media was then exchanged with media containing J591-DSPE-SIPPs (20 μg iron), IgG-DSPE-SIPPs (20 μg iron), or PBS (20 μL). The cells were incubated with the particles for 10 min at 37 °C, 5% CO_2, and the media was then aspirated, and 5.0 mL PBS was added to wash unbound particles away from the cells. Washing was repeated three times. Cover slips were mounted on slides containing a drop of ProLong® Gold Antifade Reagent with DAPI (Invitrogen, Eugene, OR). Confocal Images were acquired using a 60X oil objective with an Olympus IX-81 inverted spinning disk confocal microscope. Cells were also imaged by light microscopy, using a Zeiss Axiovert 25 CA inverted light microscope with a 63X phase-contrast objective.

Results and discussion

SIPP cores and DSPE-SIPPs were prepared as described in the "Experimental details" section. Figure 1 shows TEM images of the SIPP cores and DSPE-SIPPs. The TEM images indicate that both the SIPP cores and the DSPE-SIPPs are spherical in shape. Using ImageJ software to analyze TEM images of the SIPP cores and DSPE-SIPPs, we measured average diameters of 8.5 ± 1.6 nm and 44.2 ± 13.1 nm, respectively. DLS was also employed to measure the size of the DSPE-SIPPs and revealed diameters of 42.9 ± 8.2 nm, showing good agreement with the diameters measured with the TEM images. In this study, we also used ImageJ to analyze the number of SIPP cores per DSPE-SIPP. We analyzed 175 DSPE-SIPPs and found that there were 7.2 ± 6.8 SIPP cores per DSPE-SIPP. The TEM images suggest that the number of SIPP cores per DSPE-SIPP is quite variable even though the

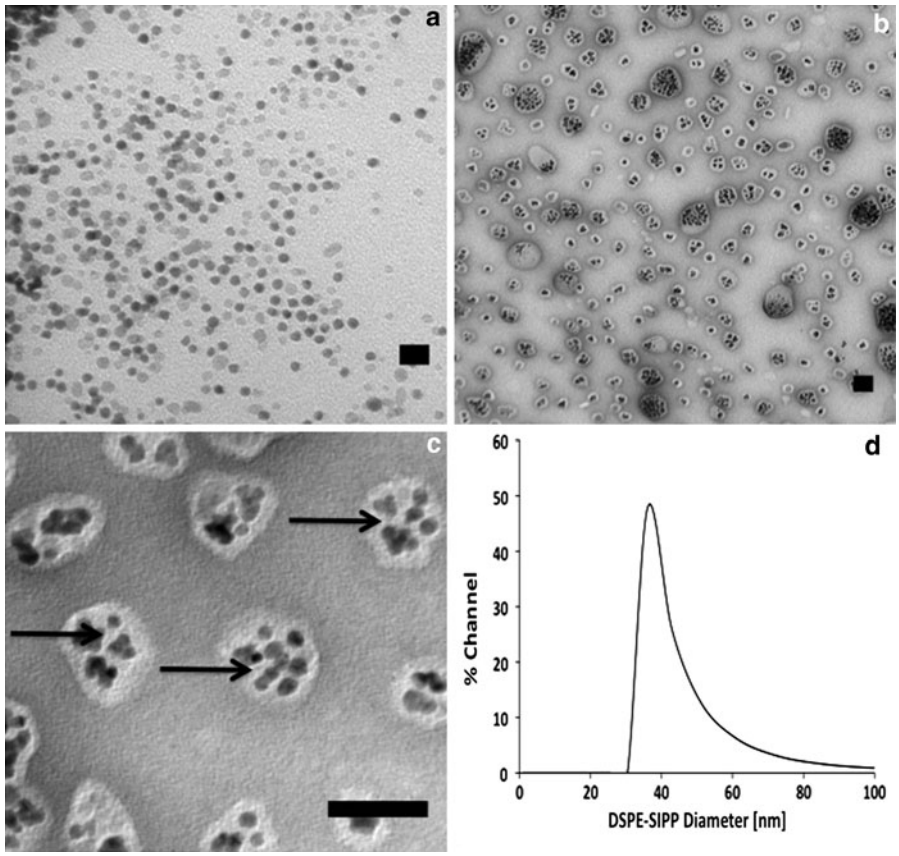

Fig. 1 TEM and DLS of SIPP Cores and DSPE-SIPPs. TEM images of **a** SIPP cores and **b**, **c** DSPE-SIPPs. *Scale bars* are 20, 50 and 50 nm, respectively. *Arrows* denote internal areas of the DSPE-SIPPs where space can be seen between the hydrophobic SIPP cores. **d** DLS of DSPE-SIPPs in PBS

overall encapsulated population is quite monodisperse, as is evident from the DLS and TEM size distribution data. Considering that the SIPP cores were found to be 8.5 nm in diameter, 5 SIPP cores would encompass a diameter of 42.5 nm, which is approximately the diameter of the DSPE-SIPPs (42.9 nm) and, on average, the greatest number of SIPP cores we observed spanning the diameter of the DSPE-SIPPs in the TEM images. This suggests that the DSPE-SIPPs do not contain an inner aqueous layer characteristic of a liposome, but rather have a purely hydrophobic inner layer that contains the hydrophobic SIPP cores. DSPE-PEG phospholipid bilayers are reported to be $\sim$5.0 nm in thickness (Johnsson and Edwards 2003). It is extremely unlikely that an 8.5 nm hydrophobic SIPP core would fit into a 5-nm bilayer. Moreover, the TEM images in Fig. 1 show that there is space in between the hydrophobic SIPP cores in the inner layer of some of the DSPE-SIPPs. It is very unlikely that water would reside at this boundary between hydrophobic phospholipid tail and hydrophobic ODA on the SIPP core surface. Therefore, we suggest that the DSPE-SIPPs are not liposomes, but rather micellar contrast agents. Johnsson and Edwards (2003) analyzed particles prepared with increasing concentrations of DSPE and DSPE-PEG and found that concentrations >33 mol% DSPE-PEG resulted in micelle formation rather than liposomes. Our DSPE-SIPPs are prepared with $\sim$98 mol% DSPE-PEG, and although liposomes and micelles reported by Johnsson and Edwards (2003) did not contain an additional hydrophobic superparamagnetic nanoparticle at the core, their results support the idea of micelle formation in our system. To investigate the stability of the DSPE-SIPP micelles, we also used TEM to image the DSPE-SIPPs up to 21 days post-synthesis. The particles were stored in PBS, pH 7.4 at 4 °C. The TEM images revealed no physical changes up to 12 days post-synthesis, at which point the DSPE-SIPPs began to merge and aggregate into larger particles (data not shown).

To investigate the composition of the SIPPs, we used ICP-OES and measured an iron to platinum ratio (Fe:Pt) of 1.24:1 for the SIPP cores. The encapsulation process did not appear to significantly affect the Fe:Pt stoichiometry. To further investigate the composition of the SIPPs and DSPE-SIPPs, TGA was used to thermally decompose the particles and determine the weight percents of ODA, phospholipid, SIPP core, and naked FePt. The thermograms of ODA, SIPPs, phospholipids, and DSPE-SIPPs are shown in Fig. 2. ODA has a boiling point around 314 °C, and both ODA and the SIPP core samples show pronounced weight loss from ~180 to 375 °C due to the removal of ODA from the SIPP surface. The hump in the middle of the curve in Fig. 2a suggests the SIPP decomposition is a two-step process. It is possible that a portion of the ODA is not bound, but rather entrapped and being removed from the particles before the bound fraction. The TGA results suggest that the organic ODA layer comprised approximately 72% of the SIPP core mass and indicated that the SIPPs were 28% naked FePt by mass. The phospholipid and DSPE-SIPP samples showed similar weight loss profiles and continued to lose mass up to ~400 °C. The DSPE-SIPP thermogram revealed that the phospholipids comprised ~55% of the DSPE-SIPP mass, while SIPP cores made up the remaining ~45% of the DSPE-SIPP mass. The mass reduction seen in the thermogram of phospholipids (prepared in chloroform) at ~65 °C is likely due to release of residual chloroform which has a boiling point of 61.2 °C.

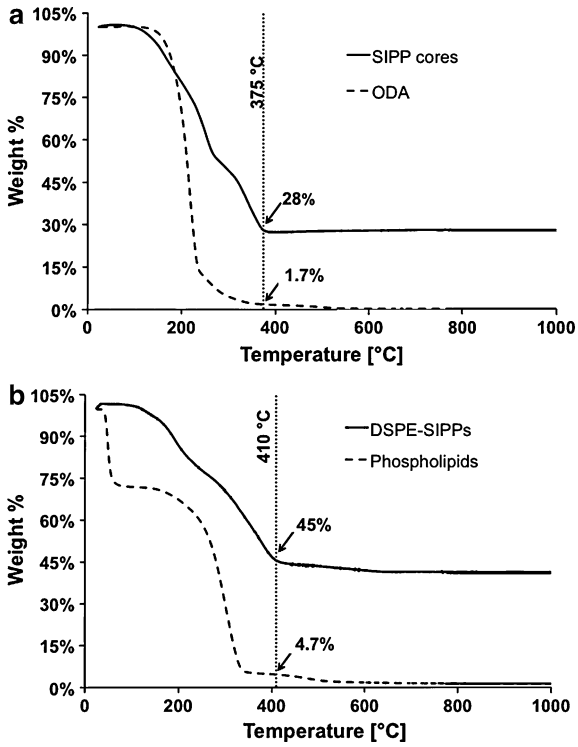

Fig. 2 SIPP Core and DSPE-SIPP TGA. TGA thermograms of **a** SIPP cores (*solid curve*) and ODA (*dashed curve*) and **b** DSPE-SIPPs (*solid curve*) and phospholipids (*dashed curve*). *Vertical dashed line* denotes the temperature, reported to the left of the *dashed line*, at which the **a** SIPP cores and **b** DSPE-SIPPs stopped loosing significant mass. % values are the percent mass of each sample remaining at the temperature denoted by the *vertical dashed line*

To characterize the magnetic properties of the SIPP cores and DSPE-SIPPs, we used SQUID magnetometry. Figure 3 shows the mass magnetization as a function of the applied magnetic field for the SIPP cores. Blank Qtips® were also scanned as controls but did not have any measureable effect in the SQUID (data not shown). The mass magnetization of the SIPP cores was 120 A m^2/kg Fe. As a comparison, we also measured commercially available SPIONs (~50 nm MACS® MicroBeads, Miltenyi Biotec) that we have previously used as an MRI contrast agent (Serda et al. 2007). The SPIONs had a mass magnetization of 82 A m^2/kg Fe, which is 1.5-fold lower than the SIPPs. SQUID magnetometry was also employed to measure the blocking temperatures

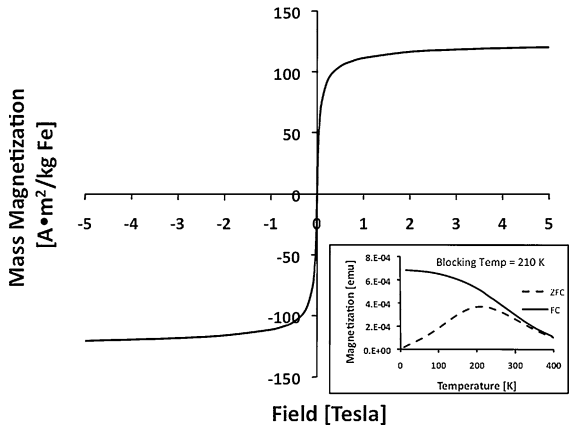

Fig. 3 Magnetization of SIPPs. Saturation magnetization curves for the mass magnetization of SIPP cores versus the applied magnetic field from −5 to 5 Tesla. *Inset* shows the zero-field-cooled (ZFC) and field-cooled (FC) curves. Values of the blocking temperature (T_B) were recorded by determining the peak location in the ZFC curve

of the SIPPs (Fig. 3), DSPE-SIPPs, and SPIONs, which were 210, 180–210, and 155 K (−63, −93 to −63, and −118 °C), respectively. All of these blocking temperatures are below body temperature, and no hysteresis is seen in the magnetization curves confirming the SIPPs, and DSPE-SIPPs, and SPIONs are superparamagnetic for biological applications. The broad blocking transition observed upon lipid encapsulation of the SIPPs is likely caused by the varying environments of the nanoparticles within the micelle, which alters the effective anisotropy energy of the particles. It has been shown that packing multiple magnetic cores into a single particle alters the measured anisotropy of the particles (Schaller et al. 2010). Next, we calculated the effective anisotropy of the SIPPs and SPIONs based on the blocking temperatures. The relationship between the effective anisotropy energy and the blocking temperature is $K = \frac{25kT_B}{V}$, where k is Boltzmann's constant, T_B is the blocking temperature, and V is the volume of the magnetic core in units of m^3. The constant 25 is calculated using a relaxation time of 1×10^{-9} s and a measurement time of 100 s. Table 1 summarizes the physical and magnetic characteristics of the SIPP cores, DSPE-SIPPs, and SPIONs and shows that the SIPPs effective anisotropy energy is ~2-fold greater than for the SPIONs. The effective anisotropy constants for the SIPPs and SPIONs are in excellent agreement with anisotropy constants for SIPP cores (Maenosono et al. 2008; Salgueirino-Maceira et al. 2004) and SPIONs (Demortiere et al. 2010; Sohn et al. 1998) previously reported.

The DSPE-SIPPs are prepared from a 56:1:1 mol ratio of DSPE-PEG, biotin-DSPE-PEG, and Liss-Rhod, respectively. The biotin-labeled phospholipid allowed us to conjugate streptavidin-labeled J591 to the DSPE-SIPPs. We measured ~2 streptavidin per J591 antibody and after conjugation, we calculated ~6 J591 antibodies per J591-DSPE-SIPP. DSPE-SIPPs were also conjugated to rabbit IgG antibodies as a non-targeted control (IgG-DSPE-SIPPs). We also measured ~2 streptavidin per IgG antibody, but ~12 IgG antibodies were measured per DSPE-SIPP. To determine if our J591-DSPE-SIPPs could specifically target PSMA-expressing human prostate cancer cell lines, we incubated the J591-DSPE-SIPPs and IgG-DSPE-SIPPs with C4-2 and PC-3 human prostate cancer cells grown on polylysine-coated cover slips. C4-2 cells were used as our PSMA-positive cell line. C4-2 is an androgen-deprivation therapy resistant cell line that over-expresses PSMA (Wolf et al. 2010; Sobel and Sadar 2005). PC-3 cells were used as a PSMA-negative cell line. PC-3 cells originate from a bone metastasis, are androgen-deprivation therapy resistant, and do not express or only minimally express PSMA (Kuroda et al. 2010; Sobel and Sadar 2005). Figure 4 shows the confocal microscopy images of C4-2 and PC-3 cells incubated with PBS (mock), J591-DSPE-SIPPs, and IgG-DSPE-SIPPs. Since the stealth immunomicelles are made with 1 mol% Liss-Rhod, the particles are fluorescent red in the confocal images. Both C4-2 and PC-3 cells lacked red fluorescence in the mock samples. Also, both cell lines only show minimal non-specific or

Table 1 Physical and magnetic characterizations of SIPPs, DSPE-SIPPs, and MACS® MicroBeads

Symbol	Variable	Units	SIPP Cores	DSPE-SIPPs	MACS®
D	Mean diameter	nm	8.5	42.9	50[a]
σ	Standard deviation of diameter	nm	1.6	8.2	–
S	Weight % solids	%	1.4	1.1	1.0
ρ	Density	g/cm^3	5.2	2.5	2.5
R	Fe:Pt ratio	–	1.24	1.27	–
C_{Fe}	Iron concentration of solution	g/mL	1×10^{-3}	5×10^{-5}	3×10^{-4}
C	Concentration of particles	Particles/mL	3×10^{16}	3×10^{14}	2×10^{14}
T_B	Blocking temperature	K	210	180–210	155
K	Effective anisotropy energy	J/m^3	2.5×10^5	2.5×10^5	1.2×10^{5b}
μ_M	Mass magnetization	A m^2/kg Fe	120	–	82

[a] Hydrodynamic diameter according to the manufacturer and (Miltenyi et al. 1990)

[b] Calculated using a magnetic core diameter of 10 nm (Miltenyi et al. 1990)

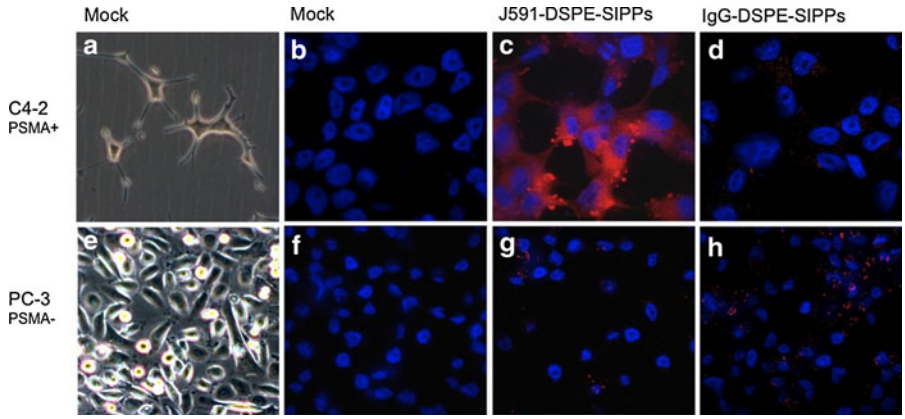

Fig. 4 Specific detection of PSMA-expressing Prostate Cancer Cells using J591-DSPE-SIPPs. C4-2 (*top row*), PSMA-positive, and PC-3 (*bottom row*), PSMA-negative, cell lines were imaged using phase-contrast light microscopy with a 63X objective (**a**, **e**). Cells were incubated for 10 min with either PBS (Mock) (**b**, **f**), J591-DSPE-SIPPs (**c**, **g**), or IgG-DSPE-SIPPs (**d**, **h**) and imaged using confocal microscopy with a 60X oil objective. *Blue* DAPI nuclear stain and *Red* Liss-Rhod incorporated in the DSPE-SIPPs

IgG-specific uptake of the IgG-DSPE-SIPPs (non targeting control). The PSMA-negative cell line, PC-3, also only showed minimal non-specific or IgG-specific uptake of the J591-DSPE-SIPPs. The amount of non-specific J591-DSPE-SIPP uptake in the PC-3 cells appears to be comparable to the non-specific uptake of the IgG-DSPE-SIPPs. In stark contrast to the other images, significant uptake of the J591-DSPE-SIPPs can be seen in the C4-2, PSMA-positive cell line. Clearly, J591-DSPE-SIPPs are internalized only by the C4-2 cell line with only minimal non-specific pick up by the PC-3 cell line and only minimal non-specific pick up when IgG-DSPE-SIPPs were used. The confocal data demonstrates the successful targeting of the multifunctional DSPE-SIPPs and detection of PSMA-expressing human prostate cancer cells in vitro with no, or minimal, non-specific binding to cell lines that do not express PSMA.

Finally, to test whether the DSPE-SIPPs could be beneficial as MRI contrast agents, we measured the longitudinal (T_1), transverse (T_2), and T_2-star (T_2*) relaxation rates of the DSPE-SIPPs and commercially available SPIONs. Table 2 shows the relaxivities measured at 4.7 Tesla, while Fig. 5 shows the T_2-weighted MR image of the DSPE-SIPP agarose samples, as well as the transverse relaxation rates of the DSPE-SIPPs and SPIONs as a function of iron concentration. It is apparent that the DSPE-SIPPs have a $\sim$13-fold higher r_2 than the SPIONs, a measure of the particles ability to create negative contrast in the MR images, and a 1.5-fold increase in the r_2/r_1 ratio. As expected, the SIPPs had increased magnetizations compared with the SPIONs and far superior transverse relaxivities. Since the commercially available SPIONs had such low transverse relaxivities, we also compared relaxivities of the DSPE-SIPPs with relaxivities of the clinically used SPION contrast agents Feridex® and Resovist® that are reported in the literature (Patel et al. 2010; Yang et al. 2010; Figuerola et al. 2008; Maenosono et al. 2008; Hinds et al. 2003). Table 3 shows the comparison of the relaxivities at 4.7 Tesla for the DSPE-SIPPs, Feridex®, and Resovist®. Compared to Feridex® and Resovist®, the DSPE-SIPPs produce superior negative contrast enhancement in MRI, as is evident from the 1.6- to 3-fold higher r_2. Overall, our data suggest that J591-DSPE-SIPPs are stable, superparamagnetic, specifically target PSMA-positive human prostate cancer cells, useful for fluorescence detection for in vitro binding applications, and superior contrast agents in T_2-weighted imaging when compared

Table 2 MR relaxivities of DSPE-SIPPs and MACS® MicroBeads at 4.7 Tesla

Sample	r_1	r_2	r_2*	r_2/r_1
DSPE-SIPPs	17	300	831	18
MACS® MicroBeads	2	23	436	12

Relaxivities are reported as s^{-1} mM^{-1}

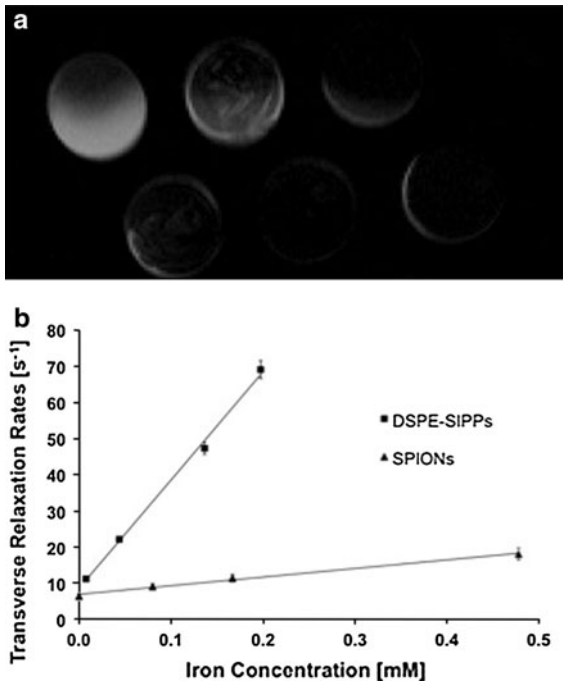

Fig. 5 Magnetic resonance relaxometry of DSPE-SIPPs and MACS® MicroBeads at 4.7 Tesla. **a** T_2-weighted MRI of 1% agarose samples containing increasing concentrations of DSPE-SIPPs. Top left sample is agarose that did not contain DSPE-SIPPs. The other samples have increasing concentrations of DSPE-SIPPs going from left to right in the top row images and continuing from left to right in the lower row images. **b** Transverse relaxation rates ($1/T_2$) versus iron concentration (mM) for the DSPE-SIPPs (*squares*) and MACS® MicroBeads (*triangles*). Linear regression was used to fit the data (*solid lines*) and the transverse relaxivities (r_n) of the DSPE-SIPPs and MACS® MicroBead SPIONs, given as the slope of the resulting line, were 300.8 ± 8.5 and 23.8 ± 6.9 s^{-1} mM^{-1}, respectively

with both commercially available and clinically used SPIONs in vitro.

Summary and conclusions

In 2009, more than 200,000 men were newly diagnosed with and over ~30,000 men died due to prostate cancer in the United States, making carcinoma of the prostate the second most lethal cancer in men in the United States (Jemal et al. 2010). New detection methods are critically needed to achieve earlier diagnosis and better staging of the disease. SPION contrast agents have been used to enhance the contrast of tumors in MRI, but novel contrast agents with increased relaxivities could be useful in detecting smaller tumors earlier and with lower doses of the contrast agents. In addition, the specific targeting of contrast agents and therapeutics to cells of interest is now widely accepted as a cornerstone to the development of individualized diagnosis and treatment. In this article, we report the synthesis of SIPP core particles from simple salts and their subsequent encapsulation in a mixture of phospholipids and conjugation to a monoclonal antibody against PSMA to produce stable, water soluble, multifunctional contrast agents with targeting, fluorescent, and MRI capabilities for the specific detection of prostate cancer cells. To our knowledge, this is the first report of the synthesis of multifunctional SIPP micelles and the first report of using SIPPs for the specific detection of prostate cancer.

Table 3 Contrast agent relaxivity comparison at 4.7 Tesla

Contrast agent	Coating	Phantom	Diameter (nm)	r_1	r_2	r_2*	r_2/r_1	Reference
DSPE-SIPPs	Phospholipid	1% Agarose	42.9	17	300	831	18	Our data
Feridex®	Dextran	2% Agarose	80–150[a]	–	148	215	–	Patel et al. (2010)
Feridex®	Dextran	2% Agarose	80–150[a]	–	–	240	–	Hinds et al. (2003)
Feridex®	Dextran	2% Agarose	80–150[a]	2.5[b]	100[b]	–	33.3	Figuerola et al. (2008)
Feridex®	Dextran	Water	80–150[a]	40	160	–	4.0	Maenosono et al. (2008)
Feridex®	Dextran	Water	80–150[a]	2.3	105	–	45.7	Yang et al. (2010)
Resovist®	Carbodextran	1% Agarose	60[a]	2.8	176	–	62.9	Yang et al. (2010)
Resovist®	Carbodextran	Water	60[a]	19.4	186	–	9.6	Maenosono et al. (2008)

Relaxivities are reported as s^{-1} mM^{-1}

[a] Wang et al. (2001)

[b] Relaxivities are estimated at 200 MHz from the graphs in the supplemental materials

The SIPP cores have a large effective anisotropy energy of 2.5×10^5 J/m^3 and magnetic moment of 120 A m^2/kg Fe. In this study, we expected that the particles with higher mass magnetizations would be better contrast agents for MRI. We found this to be true when comparing the different composition particles. Compared to the SPIONs, the SIPPs have a higher magnetization accompanied by a $\sim$13-fold higher transverse relaxivity at 4.7 Tesla. TGA suggests that the particles are $\sim$45% SIPP core and $\sim$55% phospholipid. The TEM images show that the SIPP cores and DSPE-SIPPs have diameters of 8.5 ± 1.6 nm and 42.9 ± 8.2 nm, respectively. The DSPE-SIPPs are spherical and contain 7.2 ± 6.8 SIPP cores per DSPE-SIPP. These structural characterizations suggest that the DSPE-SIPPs are micellar contrast agents. Using fluorescence confocal microscopy, we determined that the J591-DSPE-SIPPs specifically bound to C4-2 human prostate cancer cells that over-express PSMA and did not bind to PC-3 cells that do not express PSMA. In addition, IgG-DSPE-SIPPs did not accumulate in either cell line. This shows the specific detection of PSMA-expressing human prostate cancer cells using the fluorescent capabilities of the SIPP immunomicelles. Finally, we show that the DSPE-SIPPs were 13-fold better than commercially available SPIONs and 1.6- to 3-fold better than Feridex® and Resovist® at producing negative contrast in MRI, at 4.7 Tesla. Taken together, our data suggest that the multifunctional SIPP immunomicelles are superior contrast agents for T_2-weighted MRI, specifically target PSMA-expressing human prostate cancer cells, can be used to specifically detect human prostate cancer cells in vitro using fluorescence microscopy, and should be beneficial as MRI contrast agents. Future studies will include using MRI to specifically detect human prostate cancer cells in vivo using the SIPP immunomicelles. It is important to note that the DSPE-SIPPs could be conjugated to any antibody or peptide for selective targeting and non-invasive detection of other types of tumors, using MRI. An additional benefit to this multimodal platform is that the in vivo biodistribution of the nanoparticles could be measured by examining the tissues and tumors in vivo and/or ex vivo, using small animal fluorescent imagers and fluorescence microscopy. Overall, our data suggest that J591-DSPE-SIPPs specifically target human prostate cancer cells in vitro, can be easily detected using fluorescence microscopy, and are superior contrast agents in T_2-weighted MRI.

Acknowledgments The authors acknowledge the support from the National Institutes of Health 5RO1CA123194. This study was performed, in part, at the Center for Integrated Nanotechnologies, a U.S. Department of Energy, Office of Basic Energy Sciences user facility at Los Alamos National Laboratory (Contract DE-AC52-06NA25396), and Sandia National Laboratories (Contract DE-AC04-94AL85000). TEM images were generated at the University of New Mexico Electron Microscopy Facility. Confocal images were generated in the University of New Mexico & Cancer Center Fluorescence Microscopy Shared Resource, funded as detailed on: http://hsc.unm.edu/crtc/microscopy/Facility.html. Some experiments used the facilities provided by the Keck-UNM Genomics Resource, a facility supported by a grant from the WM Keck Foundation as well as the State of New Mexico and the UNM Cancer Research and Treatment Center. The authors would like to thank Dr. Stephen Jett for TEM expertise and Dr. Rebecca Lee and Genevieve Phillips for their expert guidance with confocal microscopy.

References

Afnan J, Tempany CM (2010) Update on prostate imaging. Urol Clin North Am 37 (1):23–25, Table of contents. doi: 10.1016/j.ucl.2009.11.009

Andrew W, Wender RC, Etzioni RB, Thompson IM, D'Amico AV, Volk RJ, Brooks DD, Dash C, Guessous I, Andrews K, DeSantis C, Smith RA (2010) American cancer society guideline for the early detection of prostate cancer. CA Cancer J Clin 60(2):70–98

Antoniak C, Lindner J, Spasova M, Sudfeld D, Acet M, Farle M, Fauth K, Wiedwald U, Boyen HG, Ziemann P, Wilhelm F, Rogalev A, Sun S (2006) Enhanced orbital magnetism in Fe(50)Pt(50) nanoparticles. Phys Rev Lett 97 (11): 117201–117204. doi:10.1103/PhysRevLett.97.117201

Barmak K, Kim J, Lewis LH, Coffey KR, Toney MF, Kellock AJ, Thiele JU (2004) Stoichiometry: anisotropy connections in epitaxial L10 FePt(001) films. Paper presented at the Magnetism and Magnetic Materials Conference, Anaheim, CA, USA

Basit L, Nepijko SA, Shukoor I, Ksenofontov V, Klimenkov M, Fecher GH, Schonhense G, Tremel W, Felser C (2009) Structure and magnetic properties of iron–platinum particles with y-ferric-oxide shell. Appl Phys A 94:619–625

Bhalerao GM, Sinha AK, Srivastava AK (2009) Synthesis of monodispersed gamma-Fe2O3 nanoparticles using ferrocene as a novel precursor. J Nanosci Nanotechnol 9(9): 5502–5506

Boyen HG, Fauth K, Branko S, Ziemann P, Kastle G, Weigl F, Banhart F, Hessler M, Schutz G, Gajbhiye NS, Ellrich J, Hahn H, Buttner M, Garnier MG, Oelhafen P (2005) Electronic and magnetic properties of ligand-free FePt nanoparticles. Adv Mater 17(5):574–578. doi:10.1002/adma.200400748

Chang SS, Gaudin PB, Reuter VE, O'Keefe DS, Bacich DJ, Heston WD (1999) Prostate-specific membrane antigen:

much more than a prostate cancer marker. Mol Urol 3(3):313–320

Chen S, Wang L, Duce SL, Brown S, Lee S, Melzer A, Cuschieri A, Andre P (2010) Engineered biocompatible nanoparticles for in vivo imaging applications. J Am Chem Soc 132(42):15022–15029. doi:10.1021/ja106543j

Demortiere A, Panissod P, Pichon BP, Pourroy G, Guillon D, Donnio B, Begin-Colin S (2010) Size-dependent properties of magnetic iron oxide nanocrystals. Nanoscale. doi:10.1039/c0nr00521e

Figuerola A, Fiore A, Di Corato R, Falqui A, Giannini C, Micotti E, Lascialfari A, Corti M, Cingolani R, Pellegrino T, Cozzoli PD, Manna L (2008) One-pot synthesis and characterization of size-controlled bimagnetic FePt-iron oxide heterodimer nanocrystals. J Am Chem Soc 130(4):1477–1487. doi:10.1021/ja078034v

Ghosh A, Heston WD (2004) Tumor target prostate specific membrane antigen (PSMA) and its regulation in prostate cancer. J Cell Biochem 91(3):528–539. doi:10.1002/jcb.10661

Han L, Wiedwald U, Kuerbanjiang B, Ziemann P (2009) Fe oxidation versus Pt segregation in FePt nanoparticles and thin films. Nanotechnology 20 (28):285706. doi:10.1088/0957-4484/20/28/285706

Hinds KA, Hill JM, Shapiro EM, Laukkanen MO, Silva AC, Combs CA, Varney TR, Balaban RS, Koretsky AP, Dunbar CE (2003) Highly efficient endosomal labeling of progenitor and stem cells with large magnetic particles allows magnetic resonance imaging of single cells. Blood 102(3):867–872. doi:10.1182/blood-2002-12-3669

Inomata K, Sawa T, Hashimoto S (1988) Effect of large boron additions to magnetically hard Fe-Pt alloys. J Appl Phys 64(5):2537–2540

Jemal A, Siegel R, Xu J, Ward E (2010) Cancer statistics, 2010. CA Cancer J Clin 60(5):277–300. doi:10.3322/caac.20073

Johnsson M, Edwards K (2003) Liposomes, disks, and spherical micelles: aggregate structure in mixtures of gel phase phosphatidylcholines and poly(ethylene glycol)-phospholipids. Biophys J 85(6):3839–3847. doi:10.1016/S0006-3495(03)74798-5

Kim J, Rong C, Liu P, Sun S (2009) Dispersible ferromagnetic FePt nanoparticles. Adv Mater 21:906–909. doi:10.1002/adma.200801620

Kuroda K, Liu H, Kim S, Guo M, Navarro V, Bander NH (2010) Saporin toxin-conjugated monoclonal antibody targeting prostate-specific membrane antigen has potent anticancer activity. Prostate 70(12):1286–1294. doi:10.1002/pros.21164

Lee JH, Huh YM, Jun YW, Seo JW, Jang JT, Song HT, Kim S, Cho EJ, Yoon HG, Suh JS, Cheon J (2007) Artificially engineered magnetic nanoparticles for ultra-sensitive molecular imaging. Nat Med 13(1):95–99. doi:10.1038/nm1467

Maenosono S, Suzukia T, Saita S (2008) Superparamagnetic FePt nanoparticles as excellent MRI contrast agents. J Magn Magn Mater 320:L79–L83

Miltenyi S, Muller W, Weichel W, Radbruch A (1990) High gradient magnetic cell separation with MACS. Cytometry 11(2):231–238. doi:10.1002/cyto.990110203

Morales MP, Bedard MF, Roca AG, Presa P, Hernando A, Zhang F, Zanella M, Zahoor AA, Sukhorukov GB, del Mercato LL, Parak WJ (2009) Relaxation times of colloidal iron platinum in polymer matrixes. J Mater Chem 19:6381–6386

Pasut G, Veronese FM (2009) PEGylation for improving the effectiveness of therapeutic biomolecules. Drugs Today (Barc) 45(9):687–695. doi:1396674/dot.2009.45.9.1416421

Patel D, Kell A, Simard B, Xiang B, Lin HY, Tian G (2010) The cell labeling efficacy, cytotoxicity and relaxivity of copper-activated MRI/PET imaging contrast agents. Biomaterials. doi:10.1016/j.biomaterials.2010.10.013

Peng XH, Qian X, Mao H, Wang AY, Chen ZG, Nie S, Shin DM (2008) Targeted magnetic iron oxide nanoparticles for tumor imaging and therapy. Int J Nanomedicine 3(3):311–321

Rabbani F, Stroumbakis N, Kava BR, Cookson MS, Fair WR (1998) Incidence and clinical significance of false-negative sextant prostate biopsies. J Urol 159(4):1247–1250

Rajasekaran AK, Anilkumar G, Christiansen JJ (2005) Is prostate-specific membrane antigen a multifunctional protein? Am J Physiol Cell Physiol 288(5):C975–C981. doi:10.1152/ajpcell.00506.2004

Rasband WS (1997-2009) ImageJ. US National Institutes of Health, Betesda, Maryland, USA. http://rsbinfonihgov/ij/

Salgueirino-Maceira V, Liz-Marzan LM, Farle M (2004) Water-based ferrofluids from FexPt1-x nanoparticles synthesized in organic media. Langmuir 20(16):6946–6950. doi:10.1021/la049300a

Schaller V, Wahnstrom G, Sanz-Velasco A, Enoksson P, Johansson C (2010) Determination of nanocrystal size distribution in magnetic multicore particles including dipole-dipole interactions and magnetic anisotropy: a Monte Carlo study. In: Hafeli U, Schutt W, Zborowski M (eds) Eighth International Conference on the Scientific and Clinical Applications of Magnetic Carriers, 2010. American Institute of Physics, Rostock, Germany

Serda RE, Adolphi NL, Bisoffi M, Sillerud LO (2007) Targeting and cellular trafficking of magnetic nanoparticles for prostate cancer imaging. Mol Imaging 6(4):277–288

Serda RE, Godin B, Blanco E, Chiappini C, Ferrari M (2010) Multi-stage delivery nano-particle systems for therapeutic applications. Biochim Biophys Acta. doi:10.1016/j.bbagen.2010.05.004

Sobel RE, Sadar MD (2005) Cell lines used in prostate cancer research: a compendium of old and new lines—part 1. J Urol 173(2):342–359. doi:10.1097/01.ju.0000141580.30910.57

Sohn BH, Cohen RE, Papaefthymiou GC (1998) Magnetic properties of iron oxide nanoclusters within microdomains of block copolymers. J Magn Magn Mater 182(1–2):216–224. doi:10.1016/S0304-8853(97)00675-6

Sun S (2006) Recent advances in chemical synthesis, self-assembly, and applications of FePt nanoparticles. Adv Mater 18:403

Sun S, Murray CB, Weller D, Folks L, Moser A (2000) Monodisperse FePt nanoparticles and ferromagnetic FePt nanocrystal superlattices. Science 287(5460):1989–1992

Varanda LC, Jafelicci M Jr (2006) Self-assembled FePt nanocrystals with large coercivity: reduction of the fcc-to-L1(0) ordering temperature. J Am Chem Soc 128(34):11062–11066. doi:10.1021/ja060711i

Wang YX, Hussain SM, Krestin GP (2001) Superparamagnetic iron oxide contrast agents: physicochemical characteristics and applications in MR imaging. Eur Radiol 11(11):2319–2331. doi:10.1007/s003300100908

Wolf P, Freudenberg N, Buhler P, Alt K, Schultze-Seemann W, Wetterauer U, Elsasser-Beile U (2010) Three conformational antibodies specific for different PSMA epitopes are promising diagnostic and therapeutic tools for prostate cancer. Prostate 70(5):562–569. doi:10.1002/pros.21090

Xu C, Yuan Z, Kohler N, Kim J, Chung MA, Sun S (2009) FePt nanoparticles as an Fe reservoir for controlled Fe release and tumor inhibition. J Am Chem Soc 131(42):15346–15351. doi:10.1021/ja905938a

Yang HM, Park CW, Woo MA, Kim MI, Jo YM, Park HG, Kim JD (2010) HER2/neu antibody conjugated poly(amino acid)-coated iron oxide nanoparticles for breast cancer MR imaging. Biomacromolecules. doi:10.1021/bm100560m

Zeng H, Li J, Liu JP, Wang ZL, Sun S (2002) Exchange-coupled nanocomposite magnets by nanoparticle self-assembly. Nature 420(6914):395–398. doi:10.1038/nature01208

Zhang C, Liu T, Gao J, Su Y, Shi C (2010) Recent development and application of magnetic nanoparticles for cell labeling and imaging. Mini Rev Med Chem 10(3):193–202

Zhao F, Rutherford M, Grisham SY, Peng X (2009) Formation of monodisperse FePt alloy nanocrystals using air-stable precursors: fatty acids as alloying mediator and reductant for Fe3 + precursors. J Am Chem Soc 131(14):5350–5358. doi:10.1021/ja900202t